Supporting Information

Cultivating a self-reinforcing solid-electrolyte interphase for negative-fading enhancement in $CH_3NH_3PbBr_3$ perovskite anodes

*Jia-Jie Liu,[#] Bing-Jie Feng,[#] Chen Dai, Zhi Lin, Jia-Xiong Lin, Zi-Mei Long, Ming-Jun Zhao, Li-Bing Yang, Wei-Jun Jiang, Xiao-Hui Wu**

J. J. Liu, B. J. Feng, C. Dai, Z. Lin, J. X. Lin, Z. M. Long, J. L. Huang, Z. Q. Gu, M. J. Zhao, L. B. Yang, W. J. Jiang, Prof. X. H. Wu

College of Chemistry and Materials Science, Fujian Provincial Key Laboratory of Advanced Materials Oriented Chemical Engineering, Fujian Normal University, Fuzhou 350117, China

E-mail: sherrywu@fjnu.edu.cn

Experiments

1 Materials Synthesis

1.1 Synthesis of $MAPbBr_3$ Perovskite Crystals

All chemicals were used without further purification. In a typical synthesis, 0.663 g (1.74 mmol) of lead acetate trihydrate ($Pb(CH_3COO)_2 \cdot 3H_2O$, AR grade, Aladdin) was added to a beaker. Then, 15 mL of HBr solution (≥40.0%, AR, Aladdin) and 3 mL of methylamine alcohol solution (CH_3NH_2, 27.0–32.0%, AR, Aladdin) were introduced. The mixture was stirred continuously for 15 minutes to ensure complete dissolution and homogenization. The resulting solution was transferred to a 100 mL PTFE-lined stainless-steel autoclave and heated in a blast drying oven at 150 °C for 12 hours. After natural cooling to room temperature, vacuum filtration was performed, and the product was washed three times with anhydrous isopropyl alcohol. The final product was dried in a vacuum oven at 100 °C for 12 hours, yielding pure-phase $MAPbBr_3$ crystals after natural cooling.

1.2 Thermo Treatment of CNTs

Commercially acquired carbon nanotube powder (CNT, Canrd) was placed in a beaker and heated in a vacuum drying oven at 150 °C for 12 hours. The heat-treated CNTs were collected after natural cooling to room temperature.

1.3 Preparation of MPB@CNTs Composite

As-synthesized $MAPbBr_3$ crystals and heat-treated CNT powder were mixed in a 2: 1 molar ratio. The mixture was ground thoroughly in an agate mortar for 30 minutes to ensure uniform integration. It was then transferred to a Petri dish to facilitate full exposure during heating. The sample was heated in a vacuum drying oven at 150 °C for 12 hours. After natural cooling, the final MPB@CNTs composite was obtained.

1.4 Preparation of pre-MPB@CNTs electrode

A prelithiation step was performed on the fabricated MPB@CNTs electrode. A clean lithium foil was placed onto the electrode, covered with a dust-free gasket, and pressed at about 10 N cm^{-2} for 60 seconds. After lithium foil removal, pre-MPB@CNTs electrode was obtained.

2 Electrochemical Measurements

The active material (MPB@CNTs or pre-MPB@CNTs), conductive carbon black (Super P Li), and polyvinylidene fluoride (PVDF) binder were weighed in a mass ratio of 7: 2: 1. The components were mixed and ground in an agate mortar for approximately 30 minutes, then transferred to a slurry bottle. An appropriate amount of N-methyl-2-pyrrolidone (NMP) was added to adjust viscosity. The slurry was stirred magnetically for about 6 hours until homogeneous. It was coated uniformly onto copper foil with controlled thickness. The coated foil was dried in a vacuum oven at 80 °C for 12 hours and cut into 15 mm diameter discs. A coater was used to apply the slurry uniformly onto the copper foil current collector, followed by vacuum drying at 80 °C for 12 hours. After cooling, the electrodes were cut into 15 mm discs and stored for later use.

All cells were assembled in an argon-filled glove box with oxygen and water levels below 0.01 ppm. The cell components were arranged in the following order: negative case, lithium metal sheet, electrolyte, separator, additional electrolyte, electrode sheet, gasket, spring sheet, and positive case. The assembly was sealed using a tablet press to form the final cell. Five electrolyte formulations (1) T-DME/DOL, (2) T/N-DME/DOL, (3) P/F-DEC/DMC/EC, (4) P-DMC/EC/EMC, (5) P-DEC/EC were used: (1) 1 M LiTFSI in DME: DOL (1: 1, v/v); (2) the same as (1) with 2% $LiNO_3$; (3) 1 M $LiPF_6$ in DEC: DMC: EC (1: 1: 1, v/v) with 5% FEC; (4) 1 M $LiPF_6$ in DMC: EC: EMC (1: 1: 1, v/v); and (5) 1 M $LiPF_6$ in DEC: EC (1: 1, v/v).

3 Materials Characterizations

Powder X-ray diffraction (XRD) analysis was conducted using a Rigaku X-ray diffractometer with Cu Kα radiation (λ = 1.5418 Å). Sample morphology was examined with a Hitachi SU8100 scanning electron microscope (SEM), supplemented by energy-dispersive X-ray spectroscopy (EDS) for elemental analysis. The surface and cross-section of pre-MPB@CNTs electrode sheets after 100 charge-discharge cycles at 0.1 A g^{-1} were also observed using the same SEM instrument. Contact angle measurements on cycled electrodes were performed with a Krüss GmbH instrument. X-ray photoelectron spectroscopy (XPS, Thermo ESCALAB 250XI) was used to assess the valence states of the elements.

4 Theoretical Calculations

Density functional theory (DFT) calculations were performed using Materials Studio software. Electrolyte models were constructed with the Amorphous Cell module with the following compositions: T-DME/DOL model contained 120 DME, 120 DOL, and 30 LiTFSI molecules; T/N-DME/DOL model included 120 DME, 120 DOL, 5 $LiNO_3$, and 30 LiTFSI molecules; P/F-DEC/DMC/EC model comprised 80 DEC, 80 DMC, 80 EC, 12 FEC, and 30 $LiPF_6$ molecules; P-DMC/EC/EMC model contained 80 DMC, 80 EC, 80 EMC, and 30 $LiPF_6$ molecules; and P-DEC/EC model consisted of 120 DEC, 120 EC, and 30 $LiPF_6$ molecules.

Electrode-electrolyte interface models were built using the Build Layers tool by supercell-expanding a graphene layer over $MAPbBr_3$ and merging it with a fixed electrolyte structure. Radial distribution functions and coordination numbers were derived from dynamic simulations and analytical calculations. The solvation free energy included ideal, van der Waals, and electrostatic contributions. Simulation times were ensured to be sufficient for system equilibration. Electrostatic potentials and binding energies were computed using the DMol3 module. The binding energy (E_{bind}) between solvent molecules and Li^+ ions was defined as:

$$E_{bind} = E_{total} - E_{Li^+} - E_{solvent}$$

where E_{total}, E_{Li^+}, and $E_{solvent}$ represent the total energy of the Li^+-solvent complex, the Li^+ ion, and the solvent molecule, respectively.

Molecular dynamics simulations were executed using the Forcite module with the COMPASS III force field and a 1 fs time step. Each system was equilibrated under the NPT ensemble using a Berendsen barostat at 0.1 GPa and a Nose thermostat at 298 K for over 100 ps, followed by a production run in the NVT ensemble for another 100 ps. Solvation free energy simulations were executed using the Forcite module with the COMPASS III force field and a 1 fs time step. The algorithm employs thermodynamic integration with temperature control (298 K). A production run of over 100 ps is performed under the aforementioned ensemble to reach the equilibrium state. The solvation free energy (ΔG) is obtained by summing three components: the ideal free energy, the van der Waals free energy, and the electrostatic free energy, based on the following equation:

$$\Delta G = E_{ideal} + E_{van\ der} + E_{electrostatic}$$

where E_{ideal}, $E_{van\ der}$, and $E_{electrostatic}$ represent the ideal free energy, the van der Waals free energy, and the electrostatic free energy, respectively.

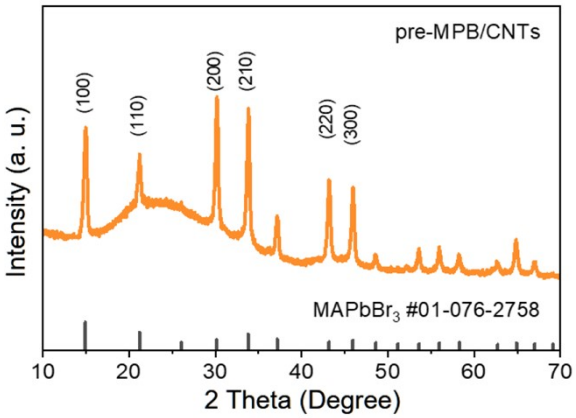

Figure S1. XRD pattern of pre-MPB/CNTs electrode in fresh.

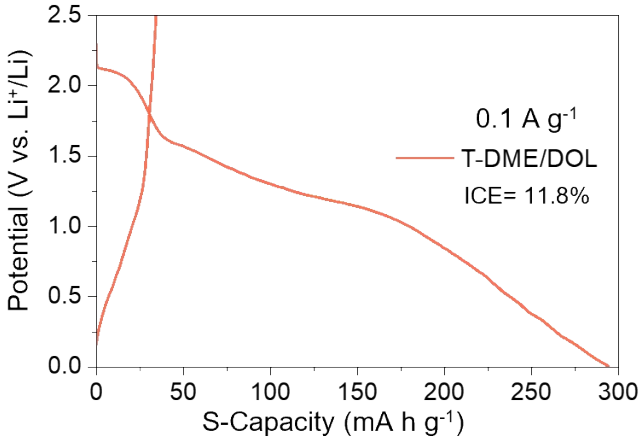

Figure S2. GCD curve of MPB/CNTs anode in T-DME/DOL electrolyte at 0.1 A g^{-1}.

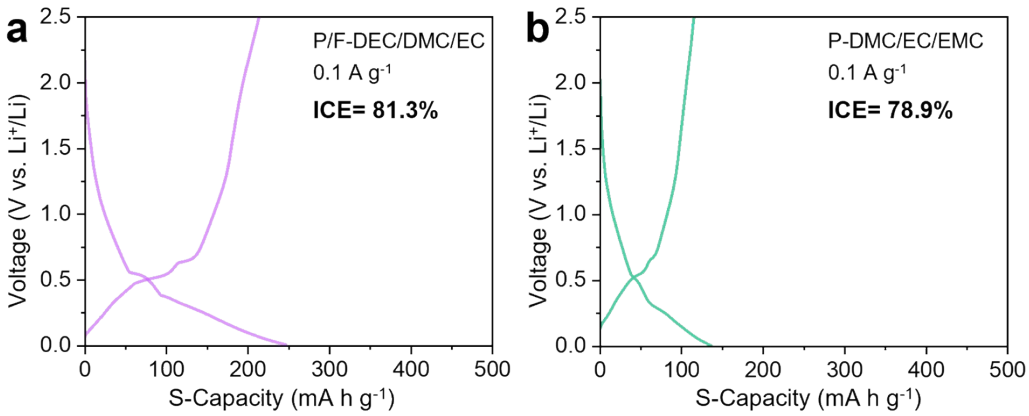

Figure S3. GCDs curves of pre-MPB/CNTs anode in two carbonate electrolytes at 0.1 A g^{-1}.

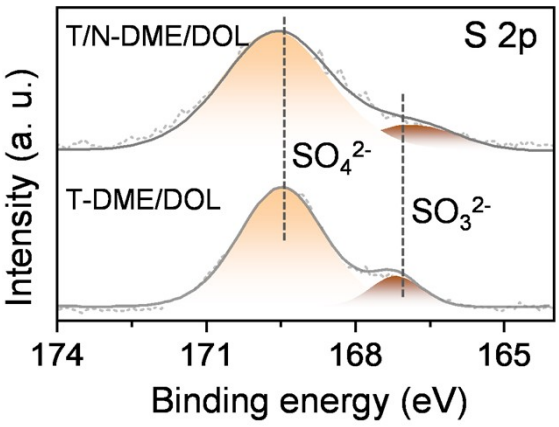

Figure S4. S 2p XPS spectra of pre-MPB/CNTs anode T-DME/DOL and T/N-DME/DOL electrolytes after the 1st cycle.

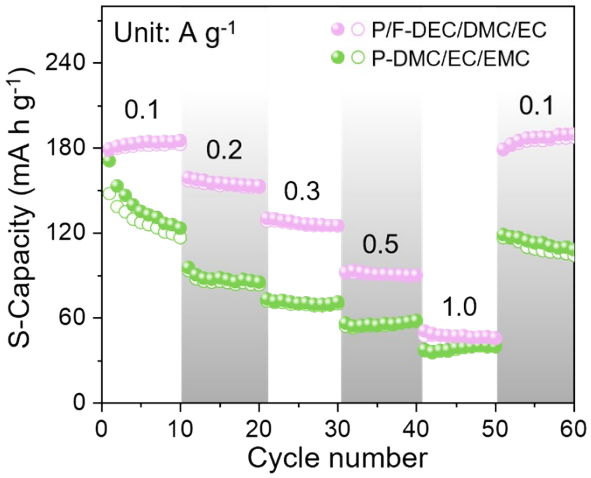

Figure S5. Rate capability of pre-MPB/CNTs anode in two carbonate electrolytes at various current densities for LIBs.

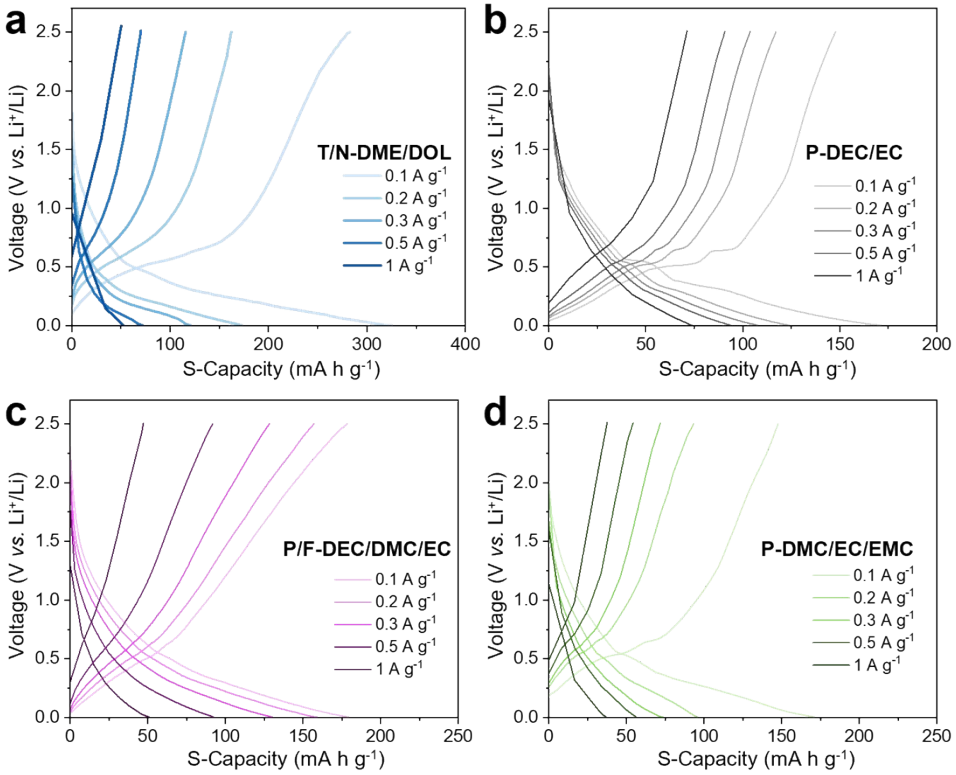

Figure S6. GCDs curves of pre-MPB/CNTs anode in four different electrolytes at different rates.

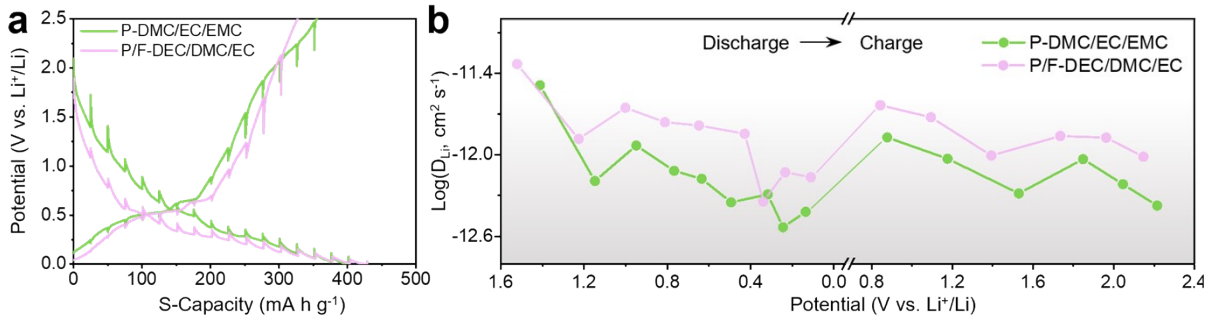

Figure S7. (**a**) GITT curves and (**b**) corresponding D_{Li} values of pre-MPB/CNTs anode in two carbonate electrolytes at discharge and charge process.

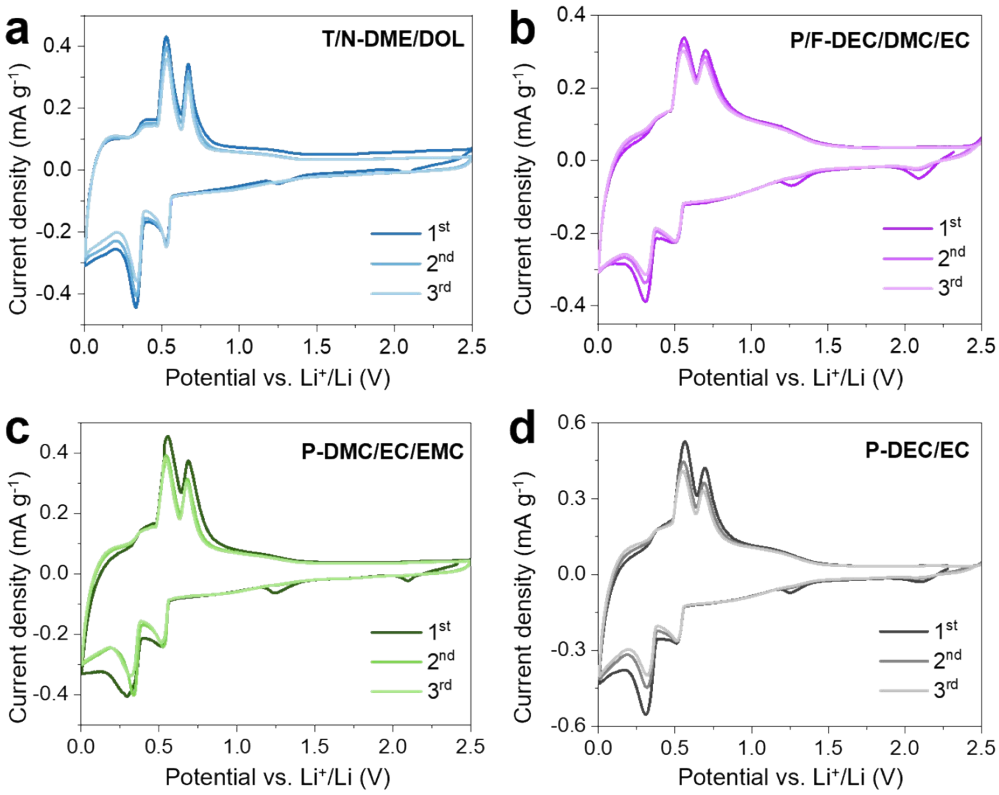

Figure S8. The initial three CV curves of pre-MPB/CNTs at 0.1 mV s^{-1} in different electrolytes: (**a**) T/N-DML/DOL, (**b**) P/F-DEC/DMC/EC, (**c**) P-DMC/EC/EMC, and (**d**) P-EDC/EC.

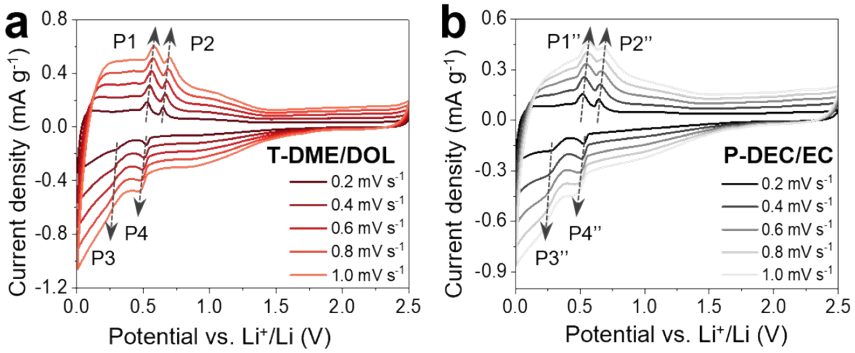

Figure S9. The CV curves of pre-MPB/CNTs in (**a**) T-DML/DOL and (**b**) P-EDC/EC at scan rates from 0.2 to 1.0 mV s^{-1}.

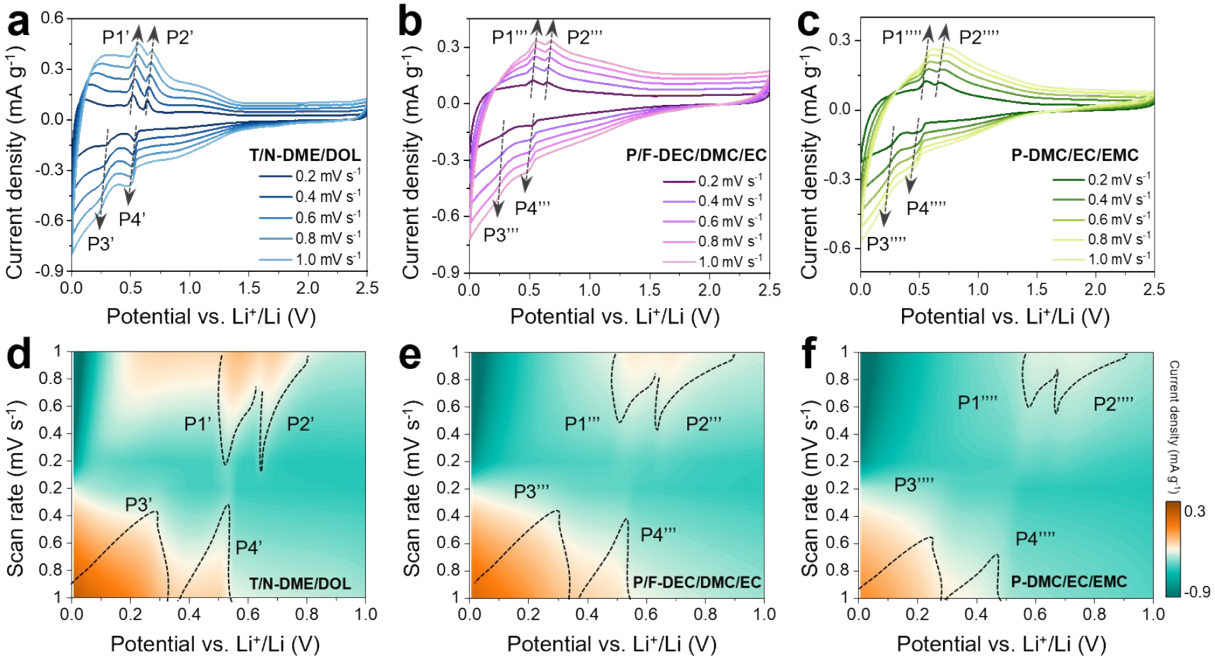

Figure S10. CV curves and corresponding contours of pre-MPB/CNTs anode in three electrolytes: (**a, d**) T/N-DML/DOL, (**b, e**) P/F-DEC/DMC/EC and (**c, f**) P-DMC/EC/EMC.

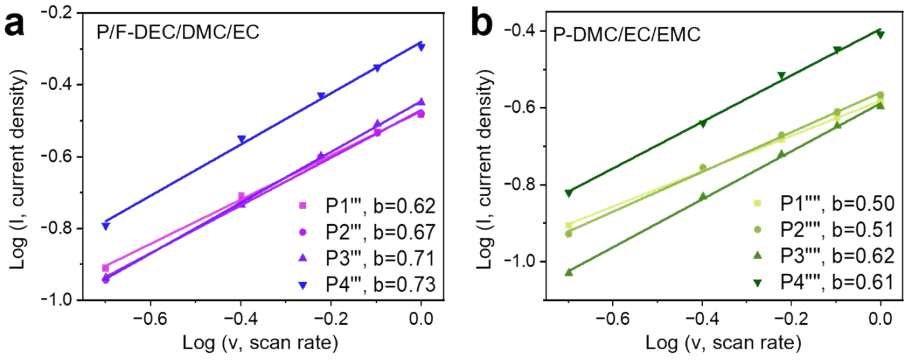

Figure S11. b-value of redox peaks in two carbonate electrolytes determined from the relation between Log(I) and Log(*v*).

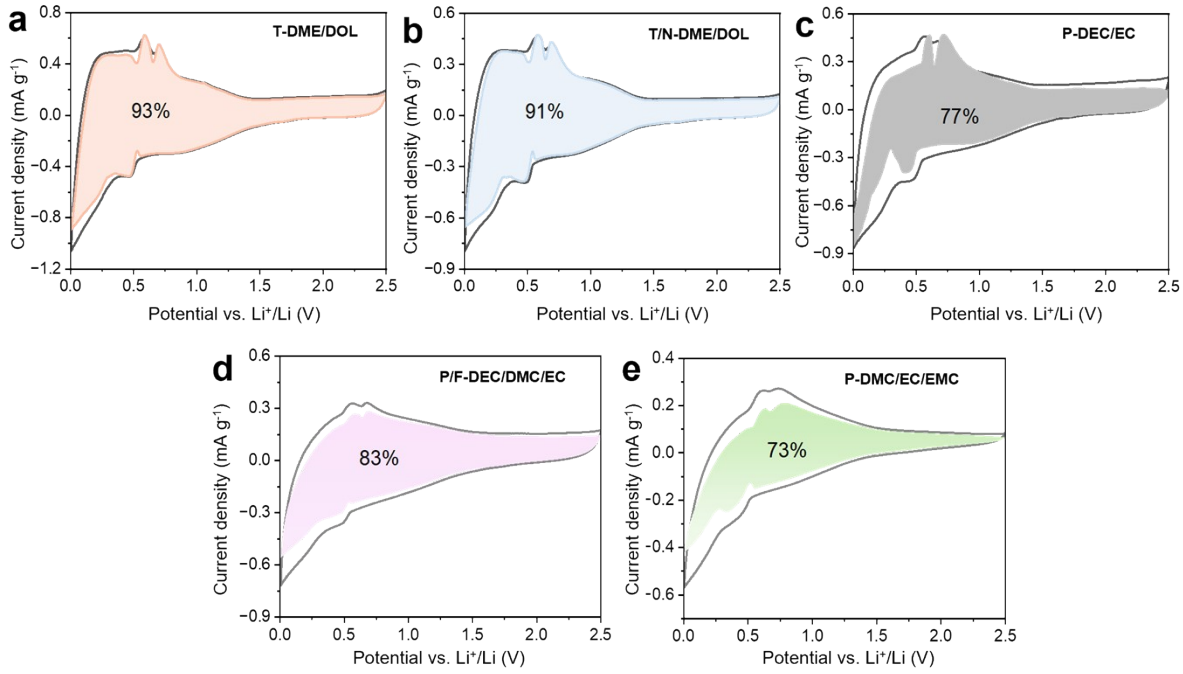

Figure S12. Capacitive contribution at 1.0 mV s^{-1} of pre-MPB/CNTs electrode in five electrolytes.

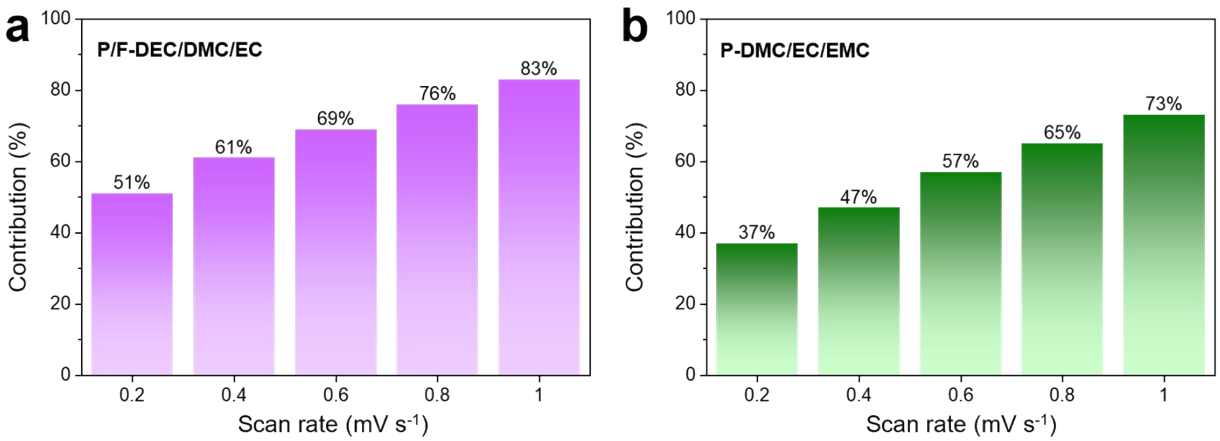

Figure S13. Capacitive contribution for Li-ion storage at different scan rates of pre-MPB/CNTs electrode in two carbonate electrolytes.

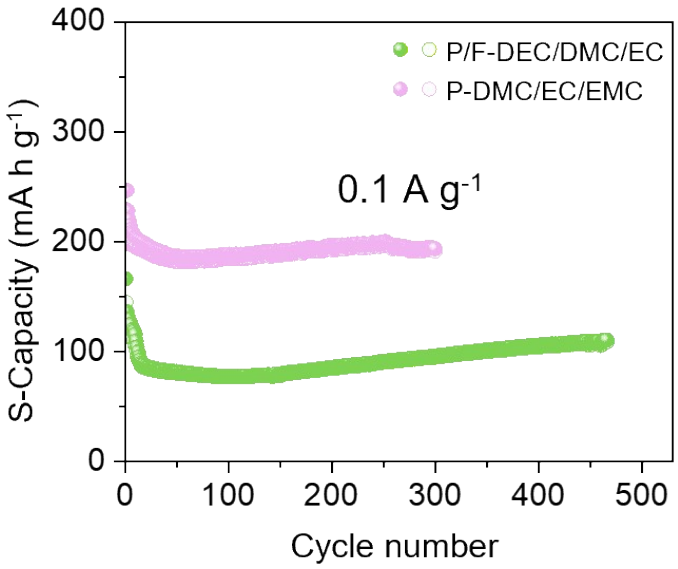

Figure S14. Cycling performance of pre-MPB/CNTs anode in two carbonate electrolytes at 0.1 A g^{-1}.

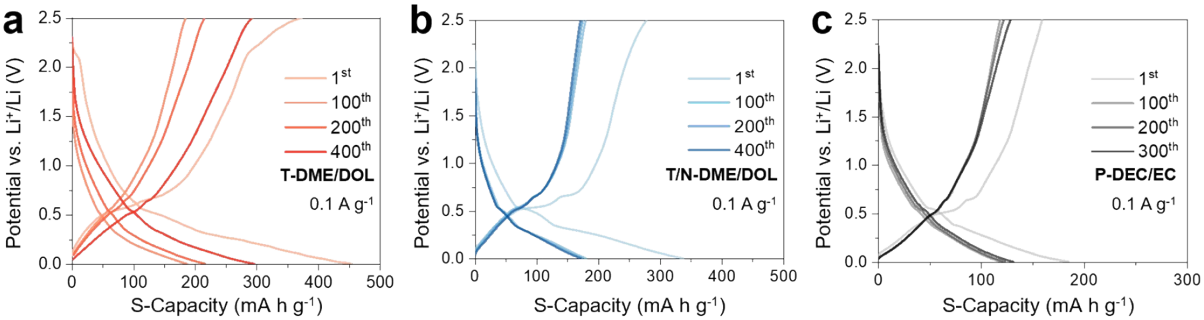

Figure S15. GCDs curves of pre-MPB/CNTs anode in three different electrolytes at different cycles.

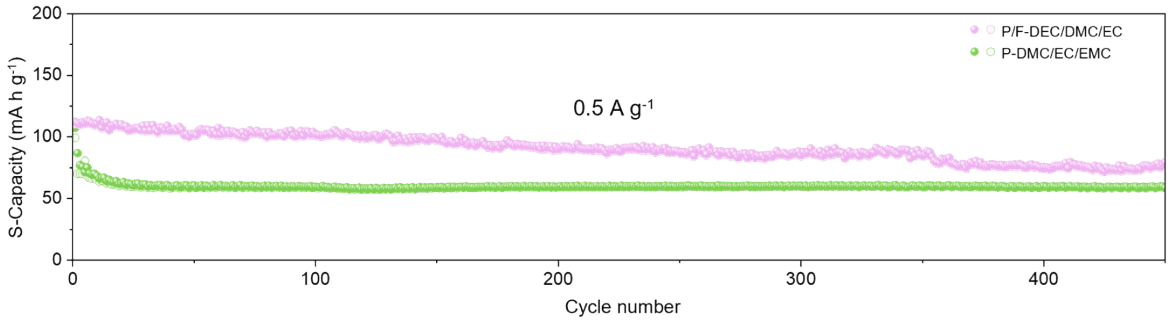

Figure S16. Cycling performance of pre-MPB/CNTs anode in two carbonate electrolytes at 0.5 A g^{-1}.

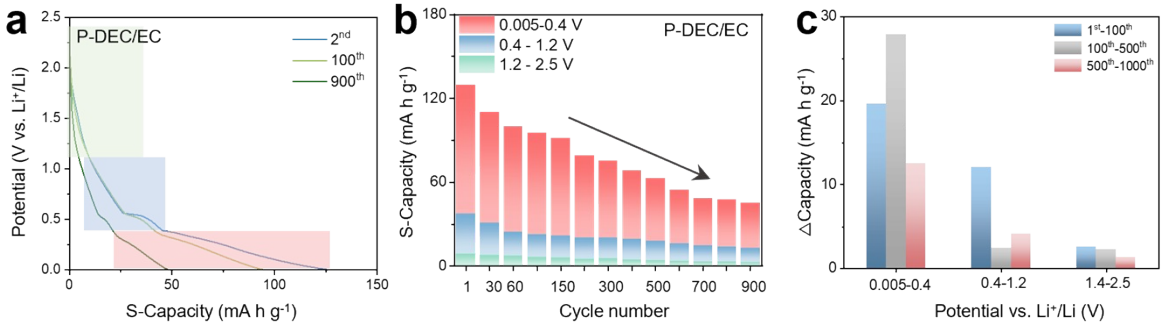

Figure S17. (**a**) The GCD curves of the pre-MPB/CNTs electrode in P-DEC/EC at 0.5 A g^{-1}. (**b-c**) Capacity changes of the pre-MPB/CNTs electrode in three voltage ranges during cycling.

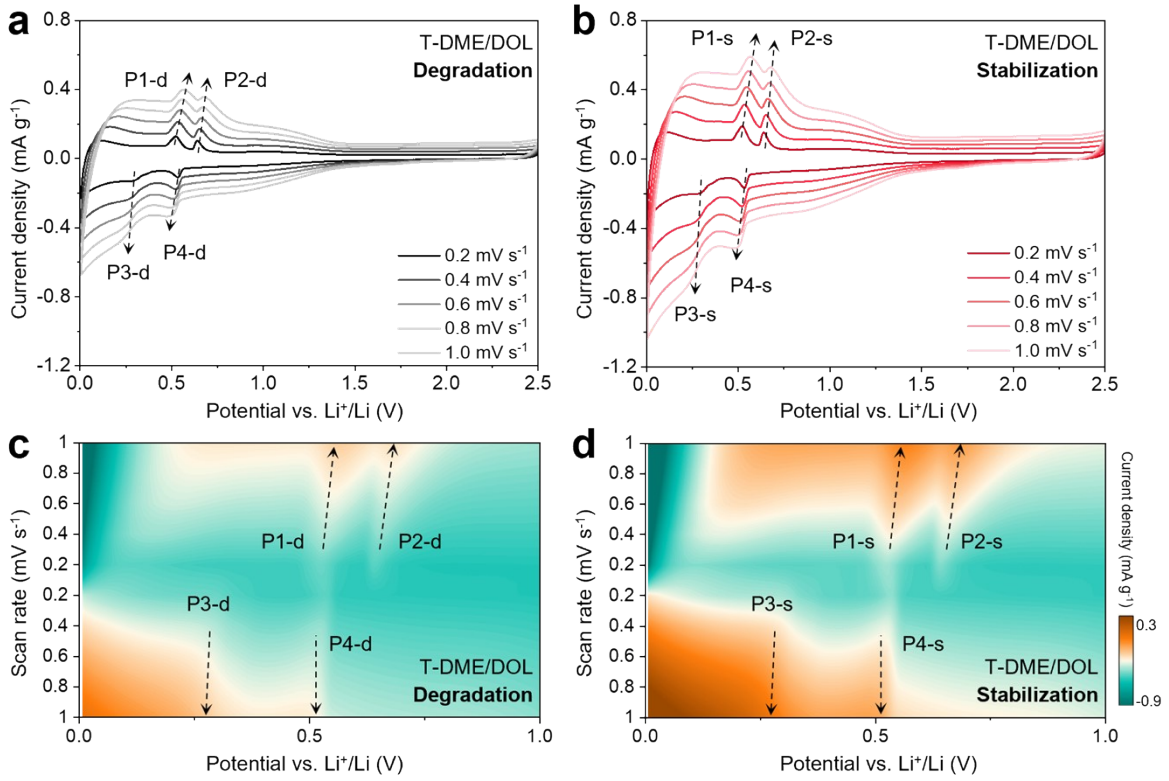

Figure S18. The CV curves and corresponding contours of pre-MPB/CNTs in T-DML/DOL (**a, c**) at the degradation status and (**b, d**) at the stabilization status at scan rates from 0.2 to 1.0 mV s^{-1}.

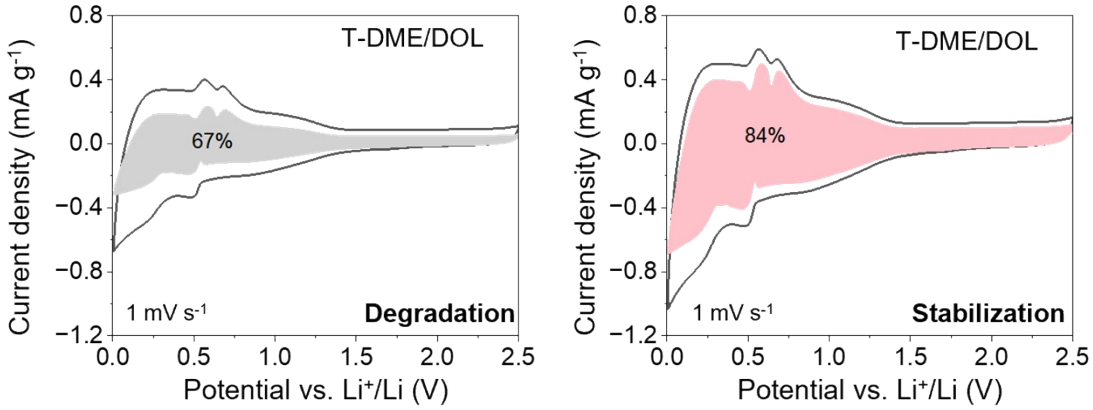

Figure S19. Capacitive contribution at 1.0 mV s^{-1} of pre-MPB/CNTs in T-DML/DOL at the degradation and stabilization status.

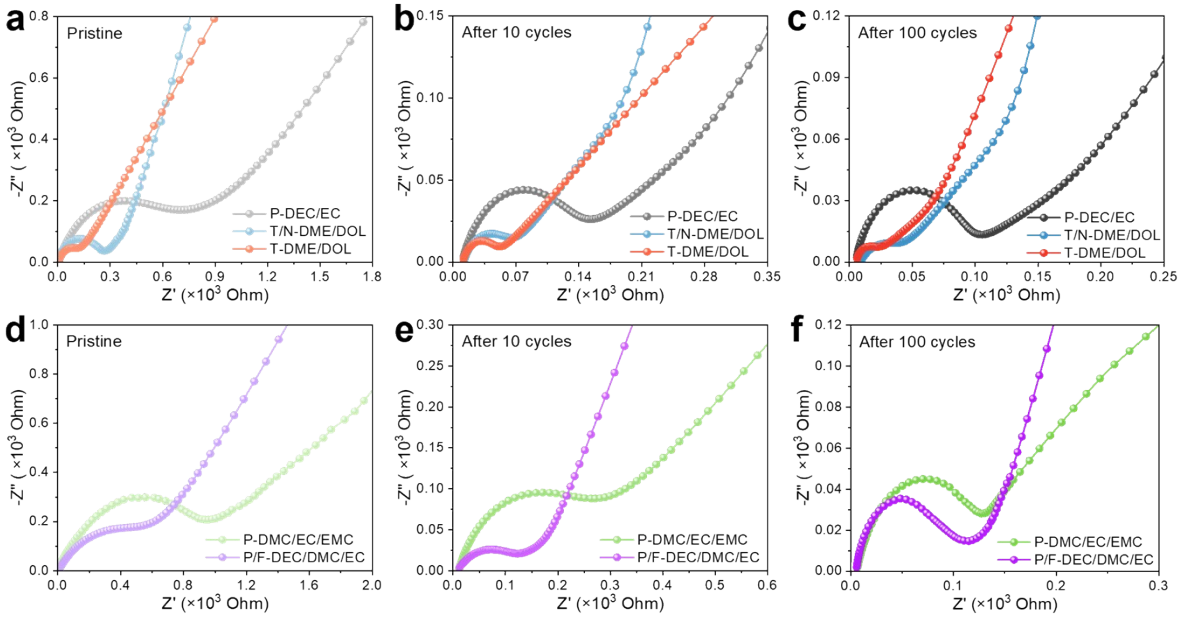

Figure S20. EIS spectra of pre-MPB/CNTs in five different electrolytes at the pristine, 10th and 100th cycles at 0.1 A g^{-1}.

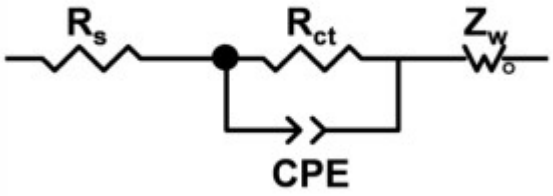

Figure S21. The fitting equivalent circuit for the Nyquist plots of the pre-MPB/CNTs electrode.

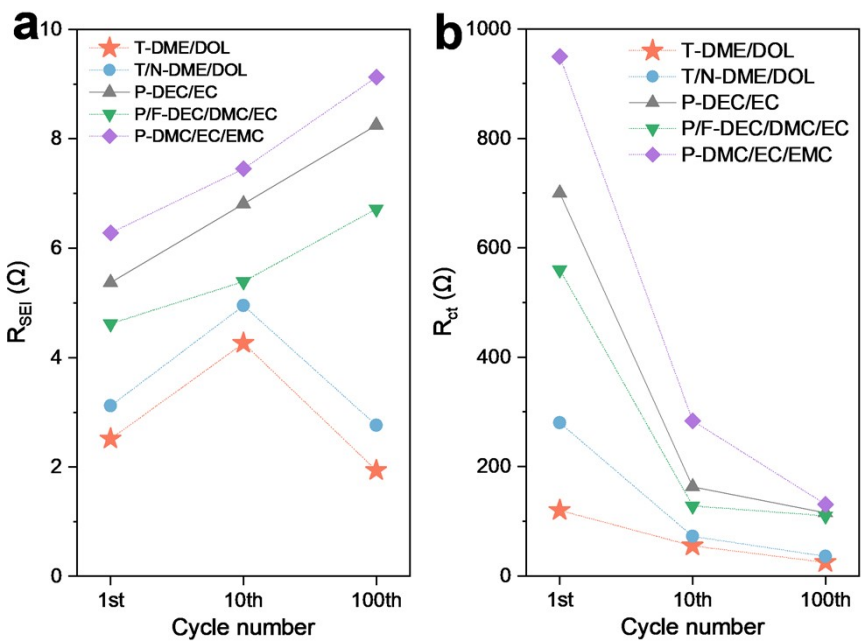

Figure S22. The fitted (**a**) R_{SEI} and (**b**) R_{ct} values of the pre-MPB/CNTs in five electrolytes.

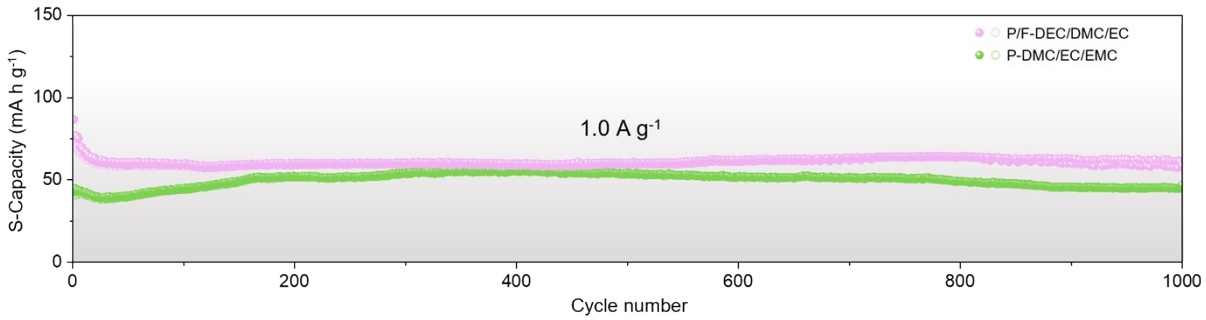

Figure S23. Cycling performance of pre-MPB/CNTs anode in two carbonate electrolytes at 1.0 A g^{-1}.

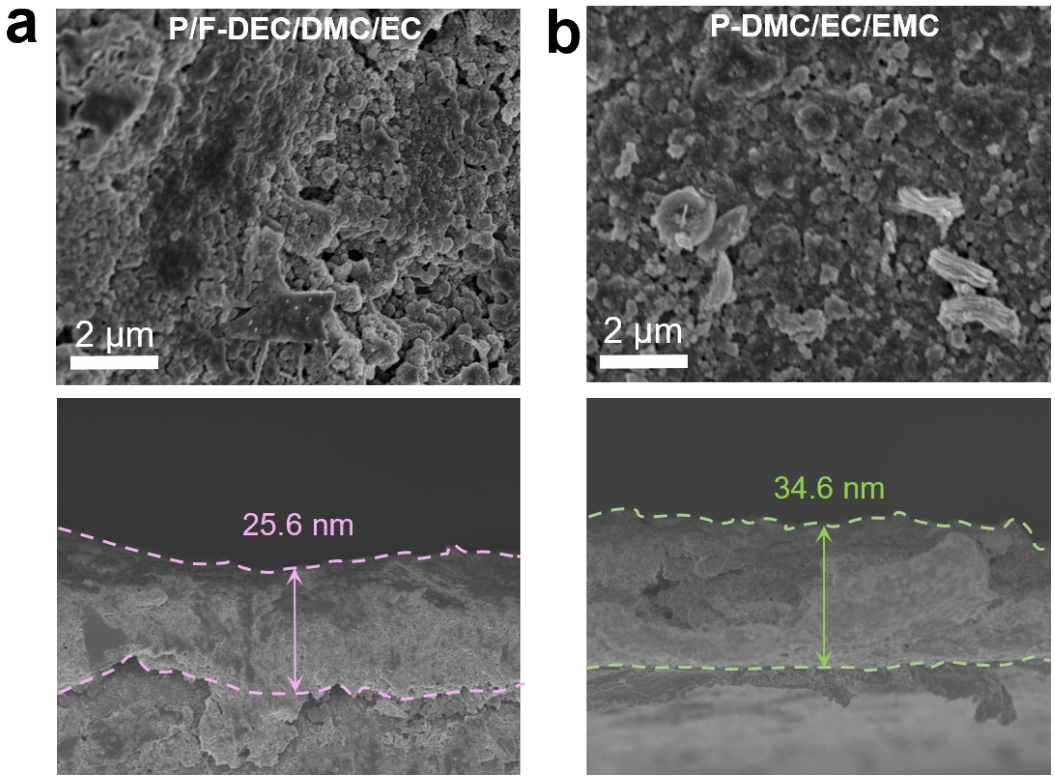

Figure S24. Planar-view and corresponding cross-sectional SEM images of the cycled pre-MPB/CNTs electrodes in (**a**) P/F-DEC/DMC/EC and (**b**) P-DMC/EC/EMC electrolytes.

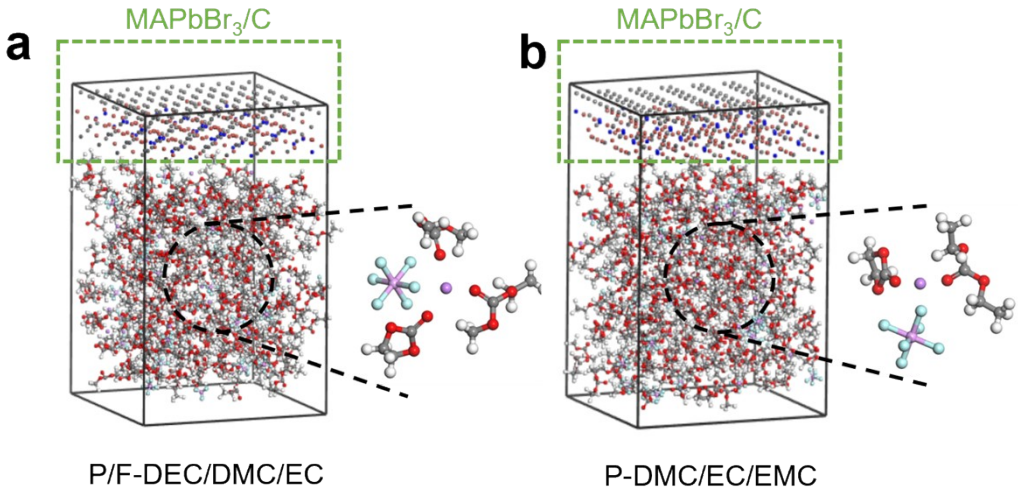

Figure S25. Models for pre-MPB/CNTs in (**a**) P/F-DEC/DMC/EC and (**b**) P-DMC/EC/EMC electrolytes.

Table S1. The specific capacity increments of the pre-MPB/CNTs electrode in three voltage ranges.

Voltage range (V)	Specific capacity (mA h g^{-1})		
	$\triangle C_{1\text{-}100}$	$\triangle C_{100\text{-}500}$	$\triangle C_{500\text{-}1000}$
0.4-0.005	84.9	-15.1	-8.5
1.2-0.4	30.11	-4.57	-1.07
3.0-1.2	6.99	-2.33	-0.43
Full range	122	-22	-10

Table S2. Comparison of cycle performance of all reported relevant $MAPbBr_3$ perovskite material composite anode (The capacity calculation is based on the whole composite).

Materials	Electrolyte	Electrochemical performance					Ref.
		Voltage Range (V)	Current density	1st discharge capacity (mA h g^{-1})	Cycle number	Specific capacity (mA h g^{-1})	
pre-MPB/CNTs	**1M LiTFSI in DME: DOL (1: 1)**	**0.005 - 2.5**	**0.1 A g^{-1}**	**453**	**400**	**300**	**Our work**
			1.0 A g^{-1}	**166**	**1000**	**159**	**Our work**
$MAPbBr_3$	1M $LiPF_6$ in EC:EMC:DMC = 1:1:1	0.01 - 1.5	0.2 A g^{-1}	331.8	200	121	1
$MAPbBr_3$	1M $LiPF_6$ in EC:EMC:DMC = 1:1:1	0.01 - 1.8	50 mC	412			2
$MAPbBr_3$	1M $LiPF_6$ in EC:DMC = 1:1:1	0.1 - 2.0	0.02 A g^{-1}	134.3			3
$(MA)_2(PA)_2Pb_3Br_{10}$	1M $LiPF_6$ in EC:DEC = 1:1	0 - 1.5	0.3 A g^{-1}	150			4
$MAPbBr_3$	1M $LiPF_6$ in EC:DEC = 1:1	0 – 1.5	0.3 A g^{-1}	330	100	150 -200	5
$MAPbBr_3$	1M $LiPF_6$ in EC:EMC:DMC = 1:1:1	0 - 1.6	0.2 A g^{-1}	200			6
$MAPbBr_3$	1M $LiPF_6$ in FEC:DEC = 1:1	0 - 1.5	0.3 A g^{-1}	164.9	1000	124	7

References:

1. Xia, H. R.; Sun, W. T.; Peng, L. M., Hydrothermal synthesis of organometal halide perovskites for Li-ion batteries. *Chemical Communications* **2015,** *51* (72), 13787-90.
2. Vicente, N.; Garcia-Belmonte, G., Organohalide Perovskites are Fast Ionic Conductors. *Advanced Energy Materials* **2017,** *7* (19), 1700710.
3. Dawson, J. A.; Naylor, A. J.; Eames, C.; Roberts, M.; Zhang, W.; Snaith, H. J.; Bruce, P. G.; Islam, M. S., Mechanisms of Lithium Intercalation and Conversion Processes in Organic–Inorganic Halide Perovskites. *ACS Energy Letters* **2017,** *2* (8), 1818-1824.
4. Ramirez, D.; Suto, Y.; Rosero-Navarro, N. C.; Miura, A.; Tadanaga, K.; Jaramillo, F., Structural and Electrochemical Evaluation of Three- and Two-Dimensional Organohalide Perovskites and Their Influence on the Reversibility of Lithium Intercalation. *Inorganic Chemistry* **2018,** *57* (7), 4181-4188.
5. Mathieson, A.; Rahil, M.; Zhang, Y.; Dose, W. M.; Lee, J. T.; Deschler, F.; Ahmad, S.; De Volder, M., Ruddlesden Popper 2D perovskites as Li-ion battery electrodes. *Materials Advances* **2021,** *2* (10), 3370-3377.
6. Zhang, L.; Miao, J.; Li, J.; Li, Q., Halide Perovskite Materials for Energy Storage Applications. *Advanced Functional Materials* **2020,** *30* (40), 2003653.
7. Wang, Q.; Yang, T.; Wang, H.; Zhang, J.; Guo, X.; Yang, Z.; Lu, S.; Qin, W., Morphological and chemical tuning of lead halide perovskite mesocrystals as long-life anode materials in lithium-ion batteries. *CrystEngComm* **2019,** *21* (6), 1048-1059.